PHYSICAL REVIEW ACCELERATORS AND BEAMS **29,** 050701 (2026)

**Editors' Suggestion**

# Data-model-guided framework for systemic emittance minimization in high-brightness photoinjectors

H. Tünnermann,[1,*] Y. Chen,[1,†] A. Klemps,[3] D. Ilia,[1,2] M. Cai,[1,2] N. Ay,[3] B. Beutner,[1]
F. Brinker,[1] W. Decking,[1] J. Good,[1] I. Hartl,[1] W. Hillert,[1,2] Y. Jiang,[1] C. Li,[1] T. Long,[1]
C. Mahnke,[1] H. Panuganti,[1] F. Pressacco,[1] and M. Scholz[1]

[1]*Deutsches Elektronen-Synchrotron DESY, Notkestraße 85, 22607, Hamburg, Germany*
[2]*University of Hamburg, Luruper Chaussee 149, 22761, Hamburg, Germany*
[3]*Hamburg University of Technology, Blohmstraße 15, 21079, Hamburg, Germany*

(Received 14 December 2025; accepted 15 April 2026; published 8 May 2026)

Bunch shaping in electron linear accelerators is of critical importance, as it enables the realization of prescribed projection profiles along specific coordinates of the bunch distribution for linac-based x-ray free-electron laser (XFEL) applications. It is evident that temporally flattop electron bunches yield more uniform slice properties, reduced emittance growth, and enhanced FEL gain compared to conventional Gaussian profiles. In this work, we present a data- and model-guided framework that consists of a physics-informed model and an inverse emittance model for minimizing the bunch emittance through laser pulse shaping and the control of laser and accelerator parameters in high-brightness photoinjectors. With a temporal flattop laser shape selected, a flat slice emittance distribution along the bunch has been experimentally obtained at the European XFEL. A measured central slice emittance of about 0.4 μm at 250 pC is achieved using a 20 ps flattop laser pulse at the photocathode. Here we present the results of a commissioning experiment, marking a practical application of temporally flattop-shaped electron bunches for stable photon delivery in a user experiment week at the facility. Within limited tuning time, a pulse energy of 1.7 mJ has been achieved at photon energies of 7.1 and 7.6 keV for the two hard x-ray undulator beamlines, surpassing the user requirements. Such a data- and model-driven framework opens up new opportunities for end-to-end optimization of machine parameters, thereby enhancing the capabilities of large-scale FEL facilities.

DOI: 10.1103/kk2s-s43l

## I. INTRODUCTION

The brightness of an x-ray free-electron laser (FEL) is critically dependent on the quality of the electron bunch that drives it, with low transverse emittance being a paramount goal. A significant source of emittance degradation arises from strong nonlinear space-charge forces within the electron bunch in the photoinjector, an effect directly tied to the initial longitudinal charge distribution. While conventional Gaussian laser pulses produce bunches susceptible to such emittance growth, temporally flattop profiles are predicted to generate a more uniform charge distribution, thereby linearizing space-charge forces and enabling better emittance preservation.

Temporal flattop picosecond pulses were generated in [1] using a passive pulse-stacking technique with multiple birefringent crystals, whereas [2] presented detailed theoretical and experimental studies of this shaping method. Using these techniques, emittance reduction of photoelectrons has been demonstrated in accelerator facilities [3–5]. Schemes for generating spatiotemporal flattop laser pulses for low-emittance photoinjectors have been studied and/or demonstrated worldwide [6–13]. Recently, a dispersion controlled nonlinear shaping method was proposed at SLAC for temporal shaping of narrow-band picosecond pulses [14] and simulations of nonlinearly shaped UV pulses were carried out for LCLS-II [15]. In China, the temporal shaping capability of the photoinjector laser system for Shenzhen superconducting soft x-ray free-electron laser (S3FEL) was reported in [16]. Generation of longitudinal flattop pulses was discussed in [17] for the Shanghai soft x-ray free-electron laser (SXFEL). While these efforts successfully established the value of temporal shaping, they also highlight a fundamental trade-off in shaping methodologies. Techniques that shape the pulse directly in the UV at high power, for instance, avoid the need for complex precompensation but are often passive or

---

[*] Contact author: henrik.tuennermann@desy.de
[†] Contact author: ye.lining.chen@desy.de

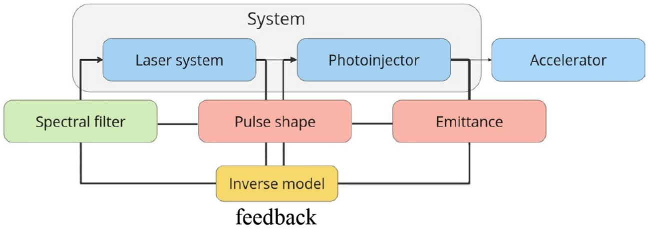

FIG. 1. Conceptual layout of the data- and model-driven emittance optimization system.

mechanically-driven, offering limited flexibility and online tunability. Conversely, shaping at the low-energy frontend offers immense versatility for generating arbitrary profiles but requires a sophisticated control strategy to precompensate for the significant nonlinear distortions in downstream amplifiers. This motivates the development of advanced adaptive control schemes that can harness the full flexibility of frontend shaping and reliably deliver any target pulse shape on demand. At the European XFEL [18], recent work has focused on adaptive, closed-loop pulse shaping and model-driven transfer of optimized profiles to the operational laser [19]. This enables the generation and precise control of arbitrary, targeted temporal pulse shapes, including flattop profiles.

In this paper, we report on an end-to-end demonstration of the temporal bunch shaping concept for photon delivery at the European XFEL user facility. We have developed and implemented a model-driven laser shaping system to generate high-fidelity flattop UV pulses at the photocathode. Subsequent injector optimization and beam characterization indicate an improved control over the slice emittance distribution along the bunch. A system layout is sketched in Fig. 1. Culminating this effort, we successfully commissioned these flattop bunches for FEL lasing, delivering the required high-intensity photon pulses for user experiments. This result validates advanced temporal shaping as a robust and practical tool for optimizing and controlling FEL performance. The paper is organized as follows. In Sec. I, a brief introduction on the proposed framework is given. Section II elucidates the temporal shaping capabilities of the cathode laser system at the European XFEL based on a physics-informed model. In Sec. III, a data-driven inverse modeling approach on the bunch slice emittance is presented. For the demonstration of the end-to-end concept, systemic optimization of the projected and sliced emittance of the electron bunch is carried out in Sec. IV, which is then followed by a dedicated FEL commissioning experiment as described in Sec. V. A conclusion and an outlook are given in Sec. VI.

## II. LASER PULSE SHAPING VIA A PHYSICS-INFORMED APPROACH

The temporal profile of the cathode laser pulse directly determines the initial longitudinal charge distribution of the electron bunch, which is a critical parameter for minimizing space-charge-induced emittance growth in the photoinjector. To generate electron bunches with a temporal flattop profile, which is highly desirable for uniform slice properties, we have developed an advanced laser system capable of producing arbitrary temporal shapes with high precision [19,20].

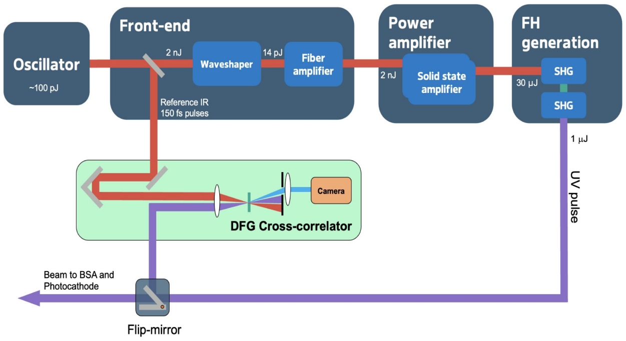

FIG. 2. Schematic of the laser pulse shaping system.

The laser is a pulsed, burst-mode system designed for photoinjector operation. The architecture, depicted schematically in Fig. 2, is based on a mode-locked oscillator that generates a train of seed pulses. These pulses are then passed through a fiber-based preamplifier stage. The core of the shaping capability is integrated within this frontend section: a commercial spatial light modulator (SLM), the waveshaper. This device operates in the frequency domain, modulating both amplitude and phase to shape the pulse. Subsequent to the frontend, the pulse train is further amplified in high-power solid-state amplifiers before undergoing two stages of second-harmonic generation (SHG) to convert the fundamental wavelength of 1030 nm to the operational UV wavelength required for photoemission from the cathode. For precise shaping, we furthermore need to be able to measure the pulse shape, which is implemented using a difference frequency generation cross correlator between a 1030 nm reference and the converted 257 nm UV beam.

The primary challenge in generating a specific temporal profile at the photocathode is that the shape programmed into the SLM is significantly distorted by the downstream optical chain. The main sources of this distortion are gain saturation in the amplifier stages, which disproportionately amplifies the leading edge of the pulse, and nonlinear effects such as self-phase modulation and SHG. To achieve the desired final pulse shape, these effects must be actively precompensated. This can be accomplished by applying an inverse transfer function of the amplifier and frequency conversion chain to the target profile at the SLM. The programmed shape is therefore intentionally predistorted such that, after undergoing the expected amplification and nonlinear evolution, it emerges as the desired clean temporal profile at the photocathode.

Determining the precise predistorted input for the SLM requires an accurate, differentiable forward model of the

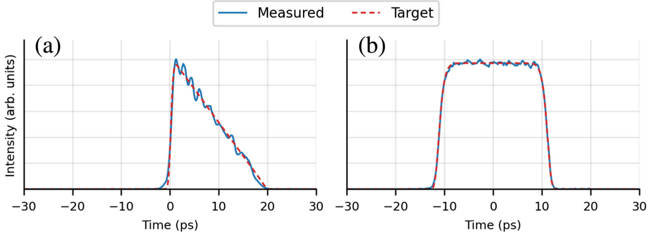

FIG. 3. Laser shape targets and resulting temporal laser shapes: (a) a semitriangle shape; (b) a flattop shape.

entire laser amplification and frequency conversion chain. To this end, we have developed a physics-informed model that simulates the pulse propagation, accounting for key effects like gain saturation, self-phase modulation, and frequency up-conversion. This model allows us to frame the task as an inverse problem: we use a gradient-descent-based optimization algorithm to iteratively adjust the spectral amplitude and phase at the SLM, minimizing the error between the model's predicted output and the desired target profile.

Recognizing that any such model is an imperfect approximation and that system conditions can drift, our method incorporates a second adaptive optimization loop. After applying a new shape and measuring the resulting UV pulse, the discrepancy between the measurement and the model's prediction is used to update the model's internal parameters, again via gradient descent. This creates an adaptive control system that not only finds the correct precompensation but also continuously refines its own accuracy. The detailed implementation of this dual-optimization framework is presented in separate publications [21].

Figure 3 illustrates this principle. The target temporal semitriangle profile (a) and flattop profile (b) are achieved by programming individually highly nonuniform, predistorted shapes into the SLM. After passing through the entire laser chain, the final measured UV pulses (blue curves) at a virtual cathode diagnostic [22] closely match the targets, demonstrating the successful compensation of all system-induced distortions and the high fidelity of our shaping technique.

## III. DATA-DRIVEN INVERSE MODELING OF EMITTANCE

The ability to precisely generate arbitrary temporal laser profiles is a critical prerequisite, but the ultimate goal is to optimize the electron bunch properties, specifically the slice emittance. To this end, we have developed a data-driven inverse model that learns the complex, nonlinear mapping from slice-emittance profile measurements to machine parameters that are the most likely to yield these measurements. This approach allows us to directly specify a desired target emittance profile and have the model predict the optimal machine settings required to achieve it.

To this end, we conducted beam dynamics start-to-end simulations executed with the simulation code ASTRA [23], uniformly varying certain simulation parameters within *a priori* defined sampling ranges derived from the usual operation regime. Those parameters are the temporal FWHM bunch length $\sigma_T$, the transverse rms spot size on the photocathode $\sigma_{xy}$, the phase $\varphi$ of the electric field in the electron gun, and the maximum on-axis field gradient of the main focusing gun solenoid $B_{\max}$. Furthermore, the simulations were conducted at a fixed charge of 250 pC and gun gradient of 57.6 MV/m assuming temporal flattop and transverse radial uniform shapes.

From a total of $n = 30\,000$ simulations, we extracted input-output pairs $\{(\mathbf{x}_i, \mathbf{y}_i)\}_{i=1}^{n}$, where $\mathbf{x}_i \coloneqq (\sigma_{T,i}, \sigma_{xy,i}, \varphi_i, B_{\max,i})$ represents the simulation inputs and $\mathbf{y}_i$ a measurement of the resulting phase space downstream of the electron source. In the course of our work, we experimented with different definitions of the measurements vector $\mathbf{y}$, which had a crucial impact on the quality of solutions to the inverse problem mapping measurements to inputs, as shown below.

Our model architecture of choice is based on an encoder-decoder neural network arrangement trained in a supervised manner on the sampled data. The *encoder* network is designed to solve the inverse problem: given a measurement $\mathbf{y}$, it predicts the corresponding operational parameters $\mathbf{x}$ that most likely have caused the measurement. The *decoder* network, conversely, learns the forward process, reconstructing the expected measurement $\mathbf{y}$ from a given set of operational parameters $\mathbf{x}$. For both encoder and decoder, the learning objectives are defined by the mean squared error between predictions and targets and are optimized independently. This dual structure allows for robust training, self-consistent validation, and the combination of surrogate models for both forward and inverse beam dynamics processes.

Since usual emittance measurements involve slicing the bunch into $N \in \mathbb{N}$ bunch slices, we first defined a measurement

$$\mathbf{y} = (z^1, \ldots, z^N, d^1 \cdot \varepsilon^1, \ldots, d^N \cdot \varepsilon^N) \tag{1}$$

as an assembly of the respective slice centers $z^1, \ldots, z^N$ with respect to the bunch center and the corresponding normalized transverse slice emittances $\varepsilon^1, \cdots, \varepsilon^N$ weighted by slice charge densities $d^1, \ldots, d^N$, emphasizing the core of the bunch. However, since emittance provides only a second-order moment description of the transverse phase space, the inverse prediction of the full bunch state from such measurements is, in general, not uniquely constrained and may therefore be partially ill-posed.

The reconstruction performance obtained using this measurement vector is shown in Fig. 4(a). The reconstruction errors across all inferred parameters are summarized using box-and-whisker plots, where the box spans the interquartile range (25th to 75th percentile), the central line

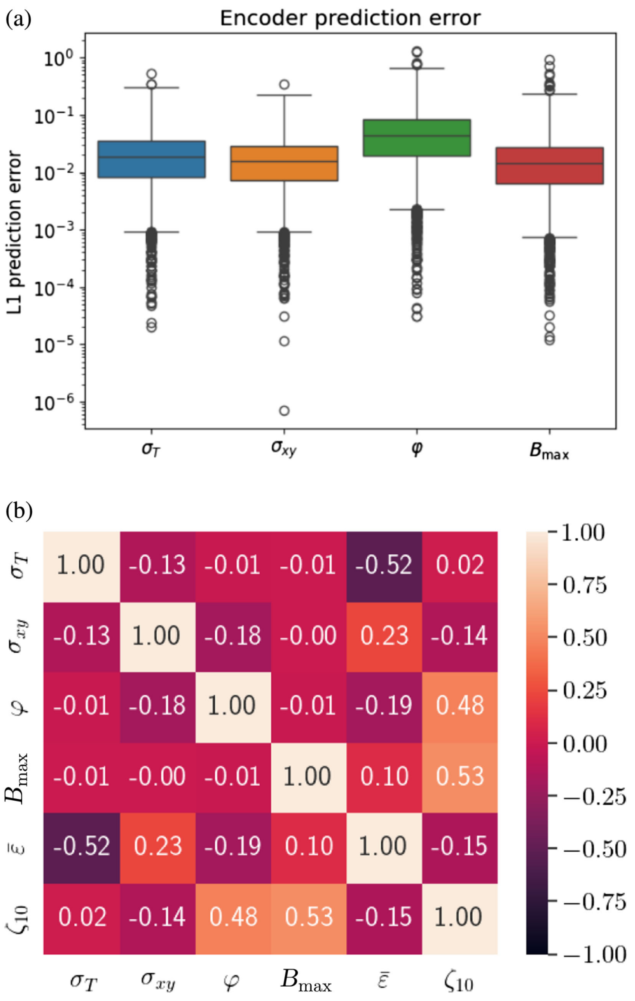

FIG. 4. Training results with measurements of shape (1). Inferring the phase $\varphi$ from emittance measurement solely is ill-conditioned due to incomplete phase space information encoded in $\mathbf{y}$, reflected by a higher prediction error. As depicted by the correlation matrix in (a), shape parameters $\sigma_T$ and $\sigma_{xy}$ show moderate correlation with the mean slice emittance $\bar{\varepsilon} := \frac{1}{N}\sum_{i=1}^{N}\varepsilon_i$, while machine parameters $\varphi$ and $B_{\max}$ better correlate with misalignments, $\zeta_{10}$ in that case. (a) L1 test encoding error distributions, (b) input-output correlations.

indicates the median, and the whiskers extend to 1.5× IQR. Figure 4(b) shows the correlations between the input parameters and the measurement vector components, confirming that the emittance-based measurements capture relevant phase space information while leaving room for further improvement in reconstruction accuracy.

In order to incorporate more phase space information into the measurements $\mathbf{y}$ without too much of an increase of input dimensionality to the inverse problem, we identified the inclusion of slice misalignments $\zeta$ [24] as a suitable option. For each slice $j \in [1, 2, \dots, N]$, $\zeta_j$ is defined as

$$\zeta_j := \frac{1}{2}[\beta_0\gamma_j - \alpha_0\alpha_j + \gamma_0\beta_i] \geq 1, \tag{2}$$

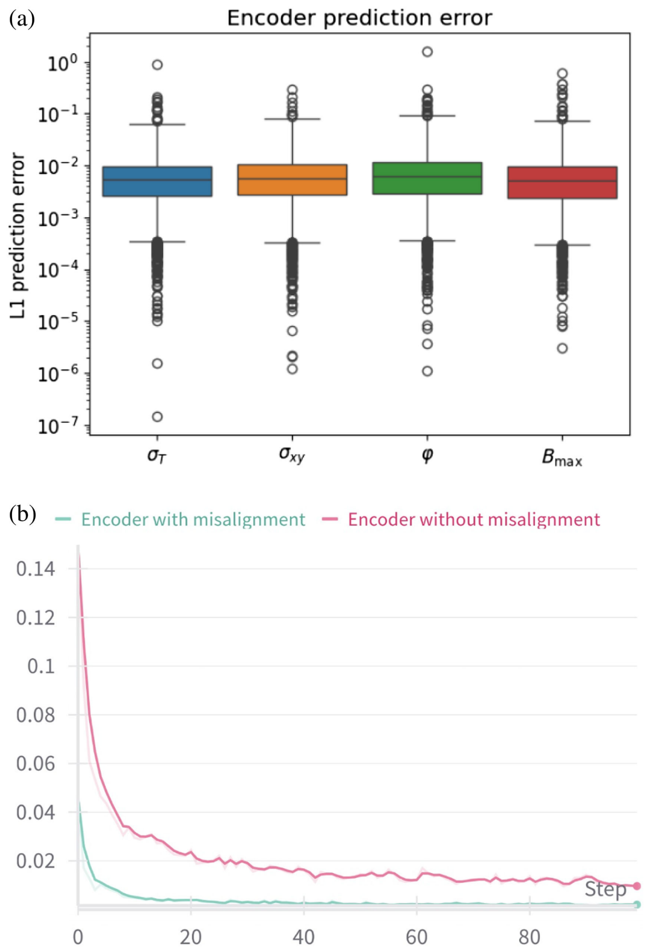

FIG. 5. Training results with inclusion of slice misalignments, yielding faster convergence and lower encoder prediction error. Without, inferring the phase $\varphi$ from emittance measurement solely is ill-conditioned due to incomplete phase space information encoded in $\mathbf{y}$. (a) L1 test encoding error distributions, (b) training convergence.

in terms of slice twiss parameters $\alpha_j, \beta_j, \gamma_j$ and bunch twiss parameters $\alpha_0, \beta_0, \gamma_0$, quantifying the misalignment of the slice phase space with respect to the whole bunch phase space. With this new extracted feature, we extended the previously defined measurements (1) to

$$\hat{\mathbf{y}} := (z^1, \dots, z^N, d^1 \cdot \varepsilon^1, \dots, d^N \cdot \varepsilon^N, d_1 \cdot \zeta^1, \dots, d^N \cdot \zeta^N). \tag{3}$$

The resulting reconstruction performance is shown in Fig. 5(a) using the same box-and-whisker representation. A systemic reduction in both the median error and the spread across parameters is observed. This improvement is further reflected in the convergence behavior during training shown in Fig. 5(b), which demonstrates faster convergence and a lower final prediction error compared to the emittance-only measurement vector.

Our experiments conducted with $N \in \{20, 40\}$ slices confirm the beneficial influence of the measurement

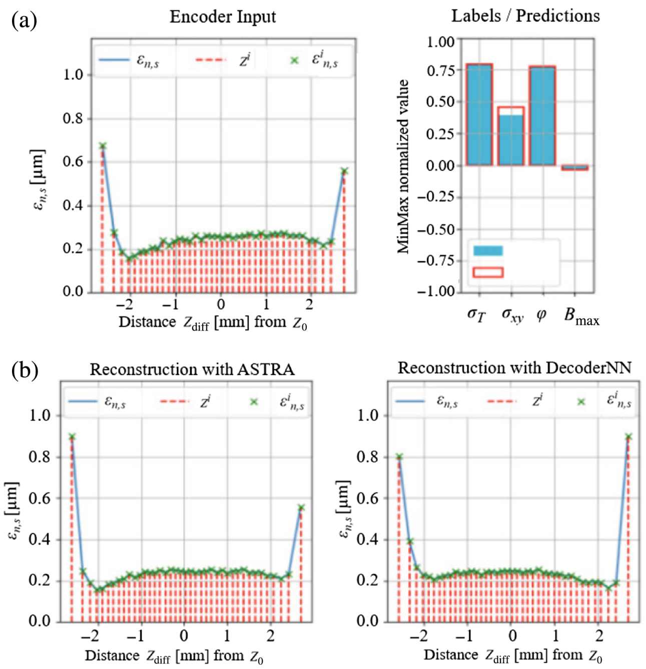

FIG. 6. Parameter prediction from test input slice profile and reconstructions with ASTRA and decoder neural network. Predicted parameters in (a) are shown normalized with respect to the boundaries of their sampling ranges and mapped to the interval $[-1, 1]$. Ground truth values for each parameter are shown as blue filled bars, predicted values as red bordered bars. The prediction error is visualized as mismatch between these. (a) Encoder parameter predictions, (b) reconstructions from predicted parameters.

extension $\hat{\mathbf{y}}$ by slice misalignments $\zeta$ on the learning process. To be precise, the modeling with extended measurements yielded (i) a faster training convergence, (ii) a decreased test prediction error by around one order of magnitude, (iii) a reduction of model complexity by approximately 50% (measured by the number of parameters) while maintaining the same prediction accuracy compared to the model with measurements $\mathbf{y}$ as defined in (1).

The predictive accuracy of the trained model is verified numerically against test simulation data not seen during training. Figure 6 demonstrates this for a target flat slice-emittance profile (a), selected from ASTRA simulations. The encoder network successfully predicts a corresponding set of operational parameters. When these parameters are used to run a new ASTRA simulation, the resulting emittance profiles [Fig. 6(b)] show excellent agreement with the original target. The model's internal decoder network also produces a consistent reconstruction, validating its grasp of the forward dynamics.

## IV. EXPERIMENTS

The combination of the adaptive laser model described in Sec. II with the inverse model on the emittance in the injector introduced in Sec. III can ultimately establish a powerful end-to-end optimization framework, capable of inversely determining the optimal laser shape and injector parameters for optimal beam quality. As a foundational step toward this goal, the work presented in this section focuses on producing a high-fidelity flattop pulse and systemically optimizing the injector performance experimentally.

A general layout of the photoinjector at the European XFEL can be found in [25]. The injector consists of a laser-driven photocathode rf gun, a post accelerating module, a third harmonic module, a laser heater, a transverse deflecting structure (TDS), a magnetic spectrometer, and other diagnostic components. The quality of temporally flattop-shaped electron bunches is characterized by their peak current, current profile, and both the transverse projected and sliced emittance. The temporal characteristics are evaluated using time-resolved measurements based on a TDS. The emittance is determined through a multiquadrupole scan technique. In combination with the TDS measurements, the transverse projected emittance of individual slices along the bunch can be resolved [26]. More detailed description on simulating the beam dynamics in the injector and verifying relevant models can be found in [22,27].

For demonstration purposes, the overall strategy first involves generating a temporally flattop-shaped cathode drive-laser pulse using the adaptive laser model, and then modeling an as-flat-as-possible slice-emittance distribution along the bunch by finely tuning the laser and injector parameters around the predicted working point of the inverse emittance model. For simplicity, the laser pulse length is fixed at about 20 ps (full width at half maximum) in these measurements. Owing to the matching-condition requirements in the injector, a systemic optimization of the transverse projected emittance, together with the matching parameter, is first performed to ensure that the central slices along the bunch are properly aligned. Note also that both lasers in the twin system at the European XFEL, X1 and X2, have been put into operation for commissioning purposes [20], and that the spatial shaping of the laser pulses, which can potentially further improve the bunch emittance, is not considered in this paper.

The obtained results are summarized in Figs. 7 and 8. Figure 7 shows the progression of experimental optimization of the transverse projected emittance using two cathode lasers (X1 and X2) and two temporal laser shapes (Gaussian and flattop) at two bunch charges (200 and 250 pC, indicated on the right axis). The upper plot presents the 100% transverse projected emittance obtained with a temporal Gaussian shape for both X1 and X2 lasers at 200 pC, and with a temporal flattop shape for the X2 laser at 200 and 250 pC. The selected bunch charge was dictated by technical considerations to ensure consistency with previous user experiments. The lower plot displays the corresponding mismatch parameter in the injector section for both the horizontal ($x$) and vertical ($y$) planes. As shown in Fig. 7, dedicated optimization using temporally flattop-shaped electron bunches yielded a projected emittance of about 0.395 µm,

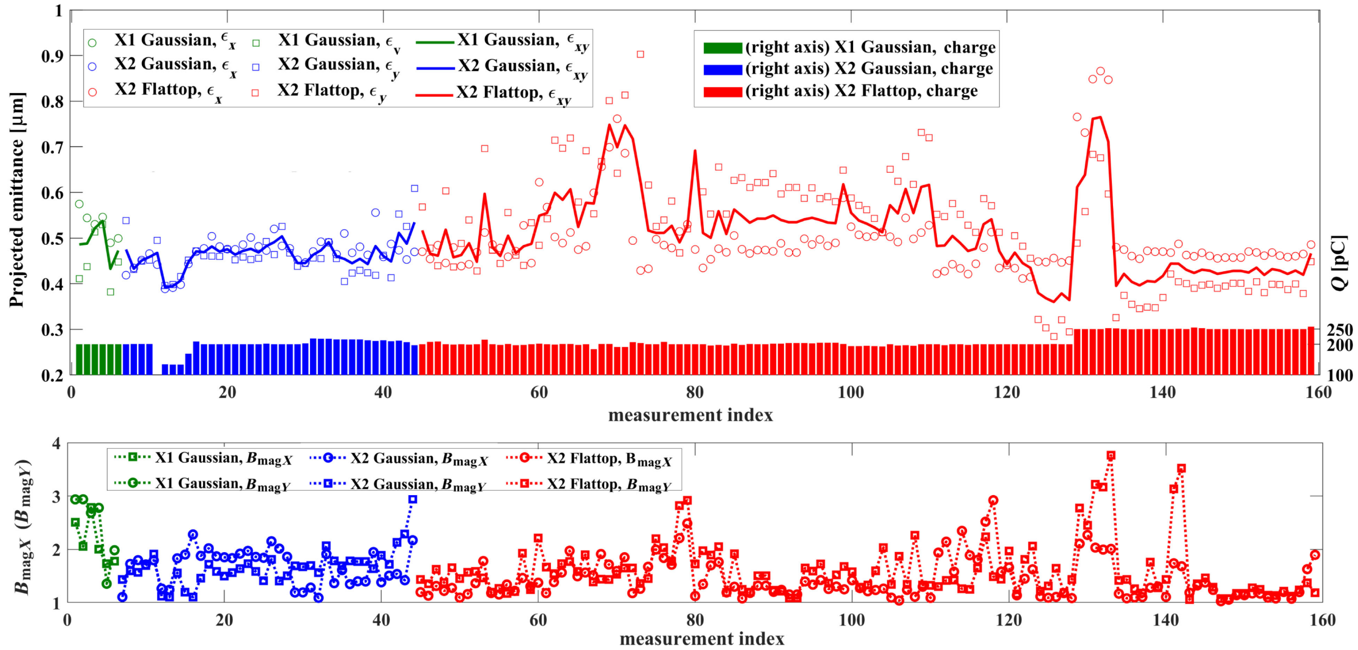

FIG. 7. Experimental optimization of projected emittance of the bunch in the injector section: history of projected emittance optimization using two cathode lasers, two temporal laser profiles, and three bunch charges: X1 Gaussian laser, X2 Gaussian laser, and X2 flattop-shaped laser (upper plot); corresponding matching parameter $B_{\mathrm{mag}}$ [24] in both horizontal ($X$) and vertical ($Y$) directions during the optimization (lower plot). Note that the mismatch parameter equal to 1 indicates a perfect matching condition.

with mismatch values of 1.4 in $x$ and 1.2 in $y$ at 250 pC. At 200 pC, the optimized projected emittance is about 0.36 μm, with mismatch values of 1.6 in $x$ and 1.1 in $y$. Compared with the optimized emittance of approximately 0.46 μm at 200 pC achieved using temporally Gaussian laser pulses during the same development week, this corresponds to an improvement of about 20% in the projected emittance, along with reductions in the mismatch parameters of 1.8 in $x$ and 1.5 in $y$ by roughly 10% and 20%, respectively.

Figure 8 illustrates the measured bunch current profiles and slice emittance for the X2 temporal flattop laser (right plot) in comparison with those obtained using the X1 temporal Gaussian laser (left plot). As shown, electrons are more uniformly distributed in the central region of the bunch for the flattop case, resulting in a flatter current profile. While the Gaussian bunch exhibits a pronounced emittance increase toward its center, the flattop bunch at the same 200 pC charge shows a significantly flatter and more

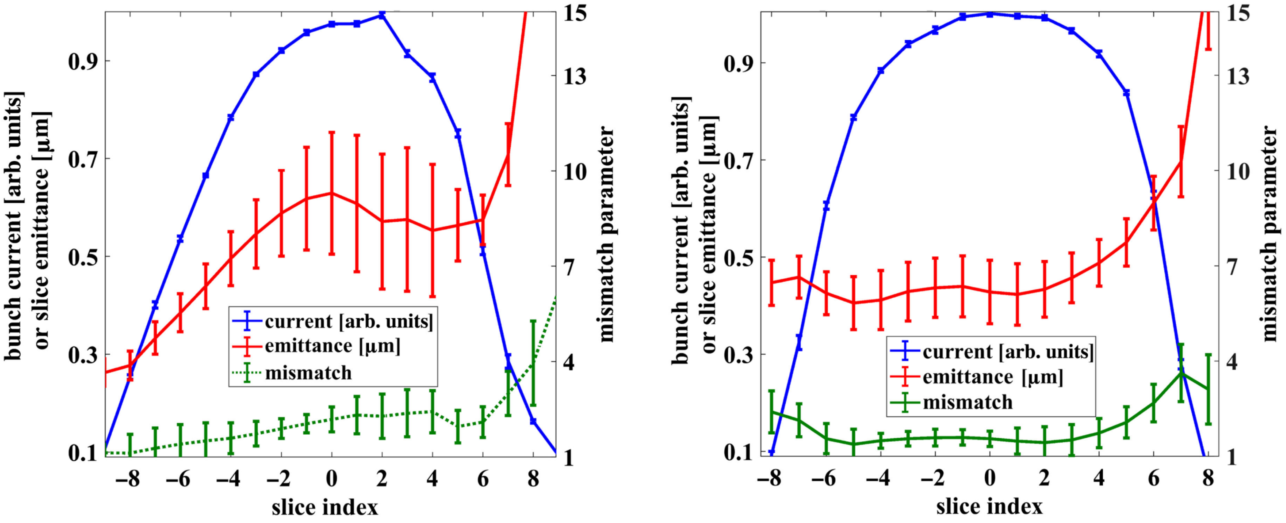

FIG. 8. Measured slice emittance in the injector for X1 temporal Gaussian laser (left plot) and X2 temporal flattop-shaped laser (right plot) at 200 pC bunch charge, respectively.

uniform slice emittance profile, with improved matching throughout. Across repeated optimization measurements, the central slice emittance for the flattop case consistently falls within the range of 0.36 to 0.49 μm. Notably, the pronounced bump in the slice emittance observed for the Gaussian case reflects enhanced space-charge effects and a strongly asymmetric distribution. Despite injector optimization, this feature persisted, likely due to transverse nonuniformities and asymmetries in the laser profile during the experiment, which further amplify space-charge-driven emittance growth. In contrast, the flattop profile mitigates these effects by providing a more uniform initial charge distribution.

As a rule of thumb, assuming the thermal emittance of cesium-telluride photocathodes manufactured using a recipe similar to that at DESY is 1.1 μm/mm (rms) [28], the intrinsic cathode emittance for a transverse uniform beam of 1 mm diameter is approximately 0.28 μm. This indicates that thermal emittance contributes approximately 60%–70% of the measured total emittance, which may already constitute a record performance for low-emittance electron beam generation at the European XFEL. The cesium-telluride photocathode used for these measurements has been in operation for many years. Over longer timescales, cathode aging effects may increasingly contribute to emittance growth and become a more significant limiting factor. It is also worth noting that the optimized characteristics of the flattop-shaped electron bunch distribution are expected to further enhance the SASE lasing process, provided that microbunching effects remain negligible under an optimized machine operating point, as observed in our experiments.

## V. FEL COMMISSIONING USING FLATTOP-SHAPED ELECTRON BUNCHES

To further validate the quality of the optimized flattop-shaped electron bunch as obtained in Sec. IV, a dedicated FEL commissioning experiment was conducted just before a user experiment week, aiming to enable robust FEL setup and lasing at the photon energies required by the users. Without significant modifications to the bunch compression stages downstream of the injector, a full-scale FEL setup along with SASE tuning was accomplished within a short time.

Figure 9 shows an optimization history of the FEL/photon pulse energy at two undulator beamlines, SASE 1 (upper plot) and SASE 2 (lower plot), respectively. A pulse energy of about 1.7 mJ has been achieved for SASE 1 at 7.1 keV photon energy and for SASE 2 at about 7.6 keV photon energy. The levels of the photon energies at two beamlines are determined by the user requirements. It should be noted that the FEL performance is not fully optimized. This is mainly due to the limited FEL tuning time that is available before the following user-run week. However, the obtained results have experimentally demonstrated that good lasing performance can be established using the flattop-shaped electron bunches. The evidence collected during the user-run week suggested a longer lasing window in the flattop case compared to nominal Gaussian laser pulses. This can be attributed to the much flatter measured slice emittance distribution along the bunch, meaning that more slices can effectively contribute to the SASE process due to their improved emittance. More importantly, the experimental results demonstrate the

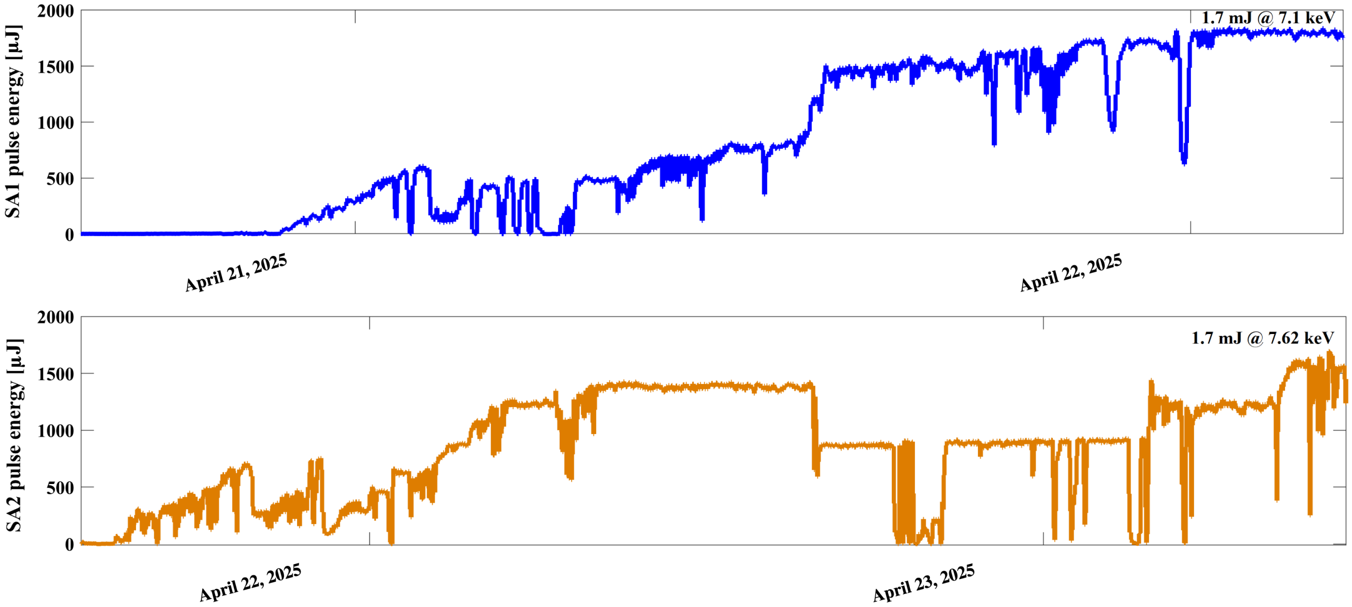

FIG. 9. Pulse energy history of short-term FEL tuning at two undulator beamlines using X2 temporally flattop-shaped cathode laser: SASE 1 undulators at about 7.1 keV photon energy (upper plot) and SASE 2 undulators at about 7.6 keV photon energy (lower plot).

effectiveness of the optimization strategy enabled by the proposed data- and model-driven framework.

In addition to the emittance improvement enabled by laser pulse shaping, we emphasize that FEL performance is ultimately determined by beam brightness and can be limited by microbunching instability (MBI) through slice energy spread (SES) growth during compression. In the present study, no evidence of enhanced MBI was observed for the flattop distribution. The adaptive laser shaping approach generates temporally smooth profiles without high-frequency modulations that could seed additional microbunching, and the finite carrier transport effects of the cesium-telluride cathode further suppress the transfer of very short-wavelength laser fluctuations to the electron beam. Moreover, both Gaussian and flattop beams were compressed with identical optics and laser heater settings, and no abnormal SES growth or compression limitations were detected. These observations indicate that, within the investigated operating regime, MBI did not limit the brightness or FEL performance of the flattop bunch. Dedicated studies on the sensitivity of different laser pulse shapes to MBI, including systemic variation of microscopic modulation spectra and compression parameters, are beyond the scope of this work and will be the subject of future investigations.

## VI. CONCLUSION

A data- and model-driven framework is proposed to minimize the electron bunch emittance through advanced laser pulse shaping and control schemes for linac-based XFELs. The approach integrates a physics-informed model that achieves a targeted temporal profile of the cathode drive-laser pulse via iterative adjustment of the SLM's spectral amplitude and phase, together with an inverse emittance model that enables a targeted slice-emittance distribution along the bunch by tuning both laser and accelerator parameters. For demonstration, temporally flattop electron bunches were generated and optimized using the proposed approach, resulting in an improvement of the transverse emittance by approximately 20%, as well as a more uniform slice-emittance distribution compared to conventional Gaussian pulses in the comparative experiments. An FEL commissioning experiment was conducted, marking the first demonstration of flattop bunches for the lasing optimization. Although the FEL performance could not be fully optimized due to limited tuning time, stable lasing with photon pulse energies of around 1.7 mJ was achieved at both hard x-ray beamlines, corresponding to user-specified photon energies of 7.1 and 7.6 keV. Further experimental studies are planned to systemically investigate the impact of laser pulse shaping on FEL pulse properties, as well as the sensitivity of different laser pulse shapes to microbunching instability.

The achieved emittance reduction is of essential importance for SASE lasing at higher photon energies in the FEL fundamental mode. Emittance improvement becomes even more critical for XFELs operating in continuous-wave mode, where the available electron beam energy is typically significantly reduced [29]. Combining the temporal shaping approach reported here with future spatial shaping techniques could further reduce the bunch emittance. Additionally, replacing the current aged cathode with a fresh one may lower the fundamental limit of the slice emittance even further. It should be noted that such a data- and model-driven framework not only enables comprehensive end-to-end optimization of machine parameters, but also represents a transformative step toward fully digitalized and intelligently controlled FEL facilities, where automated decision making will be essential for achieving unprecedented levels of performance, stability, and scientific reach.

## ACKNOWLEDGMENTS

We thank the operation teams from DESY and the European XFEL for their support. The authors gratefully acknowledge partial funding by the German Federal Ministry of Research, Technology and Space (BMFTR) through the project OPAL-FEL, Grants No. 13D22CH6, No. 05D23GT1, and No. 05D23GU3.

## DATA AVAILABILITY

The data that support the findings of this article are not publicly available. The data are available from the authors upon reasonable request.

[1] I. Will and G. Klemz, Generation of flat-top picosecond pulses by coherent pulse stacking in a multicrystal birefringent filter, Opt. Express **16**, 14922 (2008).

[2] A. K. Sharma, T. Tsang, and T. Rao, Theoretical and experimental study of passive spatiotemporal shaping of picosecond laser pulses, Phys. Rev. ST Accel. Beams **12**, 033501 (2009).

[3] S. Cialdi and I. Boscolo, A laser pulse shaper for the low-emittance radiofrequency sparc electron gun, Nucl. Instrum. Methods Phys. Res., Sect. A **526**, 239 (2004).

[4] I. V. Bazarov, D. G. Ouzounov, B. M. Dunham, S. A. Belomestnykh, Y. Li, X. Liu, R. E. Meller, J. Sikora, C. K. Sinclair, F. W. Wise, and T. Miyajima, Efficient temporal shaping of electron distributions for high-brightness photoemission electron guns, Phys. Rev. ST Accel. Beams **11**, 040702 (2008).

[5] M. Krasilnikov *et al.*, Experimentally minimized beam emittance from an $L$-band photoinjector, Phys. Rev. ST Accel. Beams **15**, 100701 (2012).

[6] C. Limborg-Deprey and P. R. Bolton, Optimum electron distributions for space charge dominated beams in photoinjectors, Nucl. Instrum. Methods Phys. Res., Sect. A **557**, 106 (2006), Energy Recovering Linacs 2005.

[7] D. Garzella, O. Gobert, P. Hollander, F. Lepetit, M. Perdrix, and T. Oksenhendler, Temporal analysis and shape control

of UV high energy laser pulses for photoinjectors, in *Proceedings of the 28th International Free Electron Laser Conference, FEL-2006, BESSY, Berlin, Germany* (2006), https://epaper.kek.jp/f06/PAPERS/THPPH001.PDF.

[8] M. B. Danailov, A. A. Demidovich, and R. Ivanov, Design of a two-stage laser pulse shaping system for FEL photoinjectors, in *Proceedings of the 28th International Free Electron Laser Conference, FEL-2006, BESSY, Berlin, Germany* (2006), pp. 617–620, https://epaper.kek.jp/f06/PAPERS/THPPH026.PDF.

[9] H. Tomizawa, H. Dewa, H. Hanaki, and F. Matsui, Development of a yearlong maintenance-free terawatt Ti: Sapphire laser system with a 3d UV-pulse shaping system for THG, Quantum Electron. **37**, 697 (2007).

[10] F. Zhou, D. Bohler, Y. Ding, S. Gilevich, Z. Huang, H. Loos, D. Ratner, and S. Vetter, Characterizing and optimizing photocathode laser distributions for ultra-low emittance electron beam operations, Reports No. SLAC-PUB-16436, No. SLAC-PUB-16491, SLAC National Accelerator Laboratory, 2015, https://www.slac.stanford.edu/pubs/slacpubs/16250/slac-pub-16491.pdf.

[11] Z. Zhang, Y. Ding, Z. Huang, and F. Zhou, Multiplexed photoinjector optimization for high-repetition-rate free-electron lasers, Front. Phys. **11**, 1166216 (2023).

[12] S. Bettoni, M. Pedrozzi, and S. Reiche, Low emittance injector design for free electron lasers, Phys. Rev. ST Accel. Beams **18**, 123403 (2015).

[13] E. Prat, P. Dijkstal, M. Aiba, S. Bettoni, P. Craievich, E. Ferrari, R. Ischebeck, F. Löhl, A. Malyzhenkov, G. L. Orlandi, S. Reiche, and T. Schietinger, Generation and characterization of intense ultralow-emittance electron beams for compact x-ray free-electron lasers, Phys. Rev. Lett. **123**, 234801 (2019).

[14] R. Lemons, N. Neveu, J. Duris, A. Marinelli, C. Durfee, and S. Carbajo, Temporal shaping of narrow-band picosecond pulses via noncolinear sum-frequency mixing of dispersion-controlled pulses, Phys. Rev. Accel. Beams **25**, 013401 (2022).

[15] N. Neveu, R. Lemons, J. Duris, J. Tang, Y. Ding, A. Marinelli, and S. Carbajo, Simulation of nonlinearly shaped UV pulses in lCLS-II, Nucl. Instrum. Methods Phys. Res., Sect. A **1072**, 170065 (2025).

[16] B. Zhang, X. Li, Q. Liu, Z. Zhu, W. Zhang, Z. He, W. Liu, G. Wu, and X. Yang, High repetition-rate photoinjector laser system for S3FEL, Front. Phys. **11**, 1181862 (2023).

[17] C. Li, X. Dai, H. Deng, L. Feng, B. Liu, J. Wang, X. Wang, and W. Zhang, Photoinjector drive laser temporal shaping for Shanghai soft x-ray free electron laser, in *Proceedings of the 12th International Particle Accelerator Conference, IPAC-2021, Campinas, SP, Brazil* (JACoW, Geneva, Switzerland, 2021).

[18] W. Decking, S. Abeghyan, P. Abramian, A. Abramsky, A. Aguirre, C. Albrecht, P. Alou, M. Altarelli, P. Altmann, K. Amyan *et al.*, A MHz-repetition-rate hard x-ray free-electron laser driven by a superconducting linear accelerator, Nat. Photonics **14**, 391 (2020).

[19] D. Ilia, C. Li, U. Grosse-Wortmann, I. Hartl, Y. Jiang, C. Mahnke, H. Panuganti, F. Pressacco, H. Tavakol, and H. Tünnermann, Advanced pulse shaping for photoinjector lasers, in *Frontiers in Ultrafast Optics: Biomedical, Scientific, and Industrial Applications XXV*, SPIE Proceedings Vol. 13353 (SPIE-International Society for Optics and Photonics, Bellingham, WA, 2025), p. 133530F

[20] C. Mahnke *et al.*, Novel photocathode lasers for the hard- and soft-x-ray free electron lasers EuXFEL and FLASH, EPJ Web Conf. **307**, 04001 (2024).

[21] D. Ilia, N. Ay, I. Hartl, W. Hillert, and H. Tünnermann, Differentiable models for control of complex physical systems: A case study in laser pulse shaping, in *Proceedings of the NeurIPS Machine Learning and the Physical Sciences Workshop* (2025), https://ml4physicalsciences.github.io/2025/files/NeurIPS_ML4PS_2025_61.pdf.

[22] Y. Chen, I. Zagorodnov, and M. Dohlus, Beam dynamics of realistic bunches at the injector section of the European x-ray free-electron laser, Phys. Rev. Accel. Beams **23**, 044201 (2020).

[23] K. Floettmann, A space charge tracking algorithm, ASTRA version 4.0, https://www.desy.de/~mpyflo/ [accessed: November 30, 2024].

[24] P. Emma and W. Spence, Grid scans: A transfer map diagnostic, in *Proceedings of the Particle Accelerator Conference, San Francisco, CA, 1991* (IEEE, New York, 1991).

[25] F. Brinker, Commissioning of the European XFEL injector, in *Proceedings of the 7th International Particle Accelerator Conference, IPAC-2016, Busan, Korea* (JACoW, Geneva, Switzerland, 2016), pp. 1044–1047, 10.18429/JACoW-IPAC2016-TUOCA03.

[26] M. Scholz and B. Beutner, Electron beam phase space tomography at the European XFEL injector, in *Proceedings of the 8th International Particle Accelerator Conference, IPAC-2017, Copenhagen, Denmark* (JACoW, Geneva, Switzerland, 2017).

[27] I. Zagorodnov, S. Tomin, Y. Chen, and F. Brinker, Experimental validation of collective effects modeling at injector section of x-ray free-electron laser, Nucl. Instrum. Methods Phys. Res., Sect. A **995**, 165111 (2021).

[28] P.-W. Huang *et al.*, Single shot cathode transverse momentum imaging in high brightness photoinjectors, Phys. Rev. Accel. Beams **23**, 043401 (2020).

[29] D. Bazyl, Y. Chen, M. Dohlus, and T. Limberg, CW operation of the European XFEL: SC-gun injector optimization, S2E calculations and SASE performance, arXiv:2111.01756.